catalysts

MDPI

Article

Magnesium-Modified Co_3O_4 Catalyst with Remarkable Performance for Toluene Low Temperature Deep Oxidation

Abraham Atour Zigla [1], Tim Kox [2], Daniel Mevoa [3], Hypolite Todou Assaouka [3], Issah Njiawouo Nsangou [3], Daniel Manhouli Daawe [1], Stephane Kenmoe [2,*] and Patrick Mountapmbeme Kouotou [1,4,*]

1 National Advanced School of Engineering of Maroua, University of Maroua, Maroua P.O. Box 46, Cameroon; abrahamzigla34@gmail.com (A.A.Z.); daawemanh2007@yahoo.fr (D.M.D.)
2 Department of Theoretical Chemistry, University of Duisburg-Essen, Universitatsstr. 2, D-45141 Essen, Germany; tim.kox@uni-due.de
3 Department of Chemistry, Faculty of Sciences, University of Maroua, Maroua P.O. Box 814, Cameroon; mevoadaniel88@gmail.com (D.M.); todouassaouka@gmail.com (H.T.A.); nsangouissah2511@yahoo.com (I.N.N.)
4 Institute of Engineering Thermophysics, Chinese Academy of Sciences, Beijing 100190, China
* Correspondence: stephane.kenmoe@uni-due.de (S.K.); mkpatrick1982@gmail.com (P.M.K.); Tel.: +49-201-183-2497 (S.K.); Fax: +49-201-183-2656 (S.K.); Tel./Fax: +237-694379627 (P.M.K.)

Abstract: Co_3O_4, $MgCo_2O_4$ and MgO materials have been synthesized using a simple co-precipitation approach and systematically characterized. The total conversion of toluene to CO_2 and H_2O over spinel $MgCo_2O_4$ with wormlike morphology has been investigated. Compared with single metal oxides (Co_3O_4 and MgO), $MgCo_2O_4$ with the highest activity has exhibited almost 100% oxidation of toluene at 255 °C. The obtained results are analogous to typical precious metal supported catalysts. The activation energy of toluene over $MgCo_2O_4$ (38.5 kJ/mol) is found to be much lower than that of Co_3O_4 (68.9 kJ/mol) and MgO ((87.8 kJ/mol)). Compared with the single Co and Mg metal oxide, the as-prepared spinel $MgCo_2O_4$ exhibits a larger surface area, highest absorbed oxygen and more oxygen vacancies, thus highest mobility of oxygen species due to its good redox capability. Furthermore, the samples specific surface area, low-temperature reducibility and surface adsorbed oxygenated species ratio decreased as follows: $MgCo_2O_4$ > Co_3O_4 > MgO; which is completely in line with the catalytic performance trends and constitute the reasons for $MgCo_2O_4$ high excellent activity towards toluene total oxidation. The overall finding supported by ab initio molecular dynamics simulations of toluene oxidation on the Co_3O_4 and $MgCo_2O_4$ suggest that the catalytic process follows a Mars–van Krevelen mechanism.

Keywords: co-precipitation; magnesium; $MgCo_2O_4$ spinel; catalytic oxidation; toluene

Citation: Zigla, A.A.; Kox, T.; Mevoa, D.; Assaouka, H.T.; Nsangou, I.N.; Daawe, D.M.; Kenmoe, S.; Kouotou, P.M. Magnesium-Modified Co_3O_4 Catalyst with Remarkable Performance for Toluene Low Temperature Deep Oxidation. *Catalysts* **2022**, *12*, 411. https://doi.org/10.3390/catal12040411

Academic Editors: Anton Naydenov and Hideyuki Katsumata

Received: 21 February 2022
Accepted: 5 April 2022
Published: 7 April 2022

1. Introduction

Volatile organic compounds (VOCs), released from numerous processes at the industrial scale, are seen as the main factors responsible for the emission of photochemical smog precursors and haze [1–3]. VOCs are well known to be not only hazardous to environment, but severely harmful to human health. Therefore, reducing the emission of VOCs is today one of the biggest challenges faced by the chemical industry to satisfy stringent environmental regulations. Among VOCs, toluene represents typical aromatic compounds mostly employed as solvents as well as industrials raw materials [4]. Conversion methods of VOCs such as toluene into CO_2 and H_2O includes catalytic oxidation. This process is well established as one of the most effective and relevant techniques for the destruction of low concentrations of VOCs (<0.5 vol%) in gas pollutants [5]. The temperature required for such processes is lower than that of thermal oxidation [6], and more importantly, no secondary pollution pollutants are generated [7].

Transition metal oxide (TMOs) and supported precious metal are two main types of catalysts materials generally employed in VOCs total oxidation [8,9]. It is well established

that precious metal catalysts have the advantage of hyperactivity, however, their uses as catalysts are limited due to their high cost, poisoning tendency (by chlorine and sulphur), easy sintering and low thermal stability [10,11]. Due to their comparable activity to noble metals, low cost, resistance to poisoning and wide range of available sources as well as high thermal stability [3,12], TMOs are attracting great attention and are extensively studied as catalysts by researchers for toluene combustion [13,14]. In this respect, many oxides based on transition metals such as Cu, [15] Co, [16,17] Ce, [18,19] Mn, [20,21] V, [22,23] etc., as well as their binary mixtures, have been investigated. Among these TMOs, cobalt oxide-based catalysts emerge as potential candidate for toluene combustion [1–3]. Several investigations to point out the active sites have been performed; although a consensus has still not been reached, it has been clearly identified that Co-Based oxide exhibit remarkable performances owing to their surface oxygen vacancies (Ov) [24,25], variable valence (Co^0, Co^{2+}, Co^{3+}, Co^{4+}) implying active site as octahedral cobalt that conversely changed in the redox couple (Co^{2+}/Co^{3+}) [24,26,27], or (Co^{3+}/Co^{4+}) [28,29], as well as the active site on the (111) facet of the tetrahedral cobalt [30].

The catalytic oxidation performance of Co_3O_4 can be enhanced by diverse kinds of modifications, including partial substitution of Co^{2+} by other transition metals (Ni^{2+}, Fe^{2+}, Cu^{2+} . . .) [31–33] rare earth (Ce, La) [34] and alkali earth metal (K, Ca, Mg) [35–37]. Among the catalysts promoters, alkali earth metals are attracting much considerable attention due to their availability, low price and almost environmental friendly properties [38]. It has been reported that the catalytic conversion of N_2O could be improved after addition of calcium and magnesium in the matrix of Co_3O_4 [35–38]. However, studies addressing the application of $MgCo_2O_4$ for VOCs oxidation such as toluene are scarce. To the best of our knowledge, this is the first report on the application of Co_3O_4 modified by a small amount of Mg as a viable and promising catalyst for toluene deep oxidation.

Among the TMO_S synthesis methods, co-precipitation is the easiest and an extensively applied technic for the production of catalysts nanoparticles [39,40]. Herein, Co was partially substituted by Mg in the matrix of Co_3O_4 spinel catalyst by the co-precipitation method. The co-existence of Mg and Co could create interaction between them and could generate abundant oxygen vacancies (Ov), which is conducive to the oxygen mobility and promotes the redox cycle. Many imperfections such as lattice defects (antisites, vacancies and interstitials) might be generated and may play a determinant role in improving some physico-chemical characteristics of the host material [41]. Therefore, the impact of adding Mg into Co_3O_4 on the toluene total oxidation was studied. More importantly ab initio molecular dynamics simulations were performed to investigate the initial steps of toluene adsorption and oxygen vacancy formation on hydroxylated Co_3O_4 and $MgCo_2O_4$ (111) surface terminations.

2. Results and Discussion

2.1. Structure and Microstructure

XRD analyses were performed to identify and analyze the crystallite phases as presented in Figure 1. The X-ray spectrum of MgO exhibits signals at 2θ = 36.81°, 42.83°, 62.31° and 78.45°, which are assigned as reflections planes from the (111), (200), (220), and (222) of MgO phase (JCPDS 01-075-0477) [42]. More importantly, no other reflections from crystallographic planes were observed, attesting the purity of the obtained phase. For $MgCo_2O_4$ sample, various typical and well-defined peaks at 31.22°, 36.66°, 38.55°, 44.80°, 55.55°, 59.27°, 65.14°, and 73.31° can be indexed to (200), (311), (222), (400), (422), (511), (440), (533) and (622) crystal of bulk $MgCo_2O_4$ (PDF-02-1073), respectively. The overall peaks are in excellent agreement with previously reported data [43,44]. The diffractograms support the spinel structure of the $MgCo_2O_4$ [45,46], revealing no major structural changes upon modifications of the Co_3O_4 parent oxide. It is worth mentioning that diffraction peaks of $MgCo_2O_4$ are sharp and narrow with high intensity than those of Co_3O_4, suggesting good crystallinity of the sample. In addition, no spurious phases or other peaks ascribed to impurities were observed, revealing high purity of the overall samples. Estimation of

the grain size of the prepared catalysts from the full width at half-maximum of the most prominent peaks revealed that grain size of $MgCo_2O_4$ were smaller (22 ± 5 nm) than that of Co_3O_4 (30 ± 5 nm) and MgO (45 ± 5 nm). From Table 1 it is observed that $MgCo_2O_4$ sample with the lowest average grain size possessed the largest specific surface area of 82 $m^2 \cdot g^{-1}$, which could be attributed to the significant contribution of the existing porous structures. It is well admitted that, catalysts with higher specific surface area will provide more available active sites, which will be beneficial for the enhancement of the catalytic activity [47]. It is thus expected that, $MgCo_2O_4$ with an apparent rich porous structure and substantial specific surface area, will exhibit good performance in the total oxidation toluene. Noticeably, the average particle sizes estimated with SEM are in accordance with XRD data.

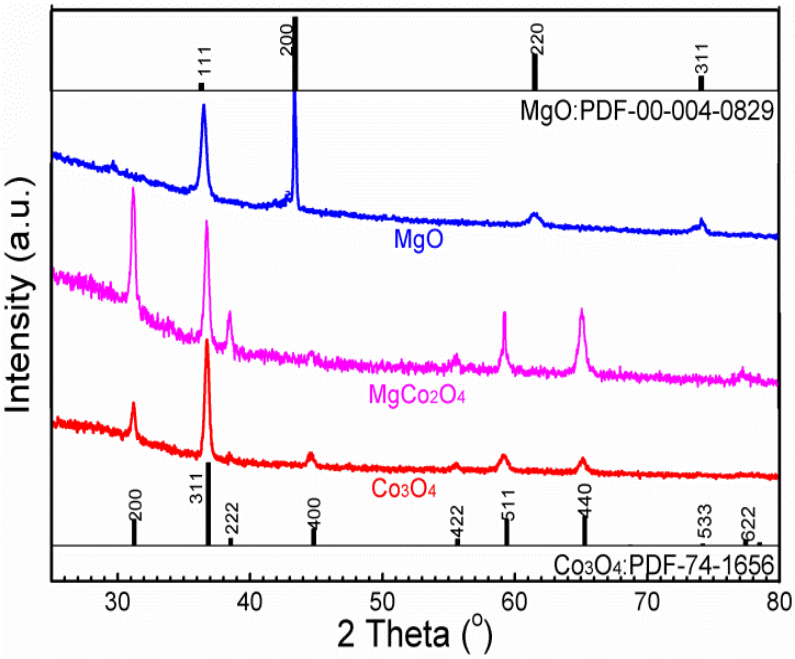

Figure 1. XRD patterns of Co3O4, MgCo2O4, and MgO samples obtained by co-precipitation.

2.2. Morphology Analysis

The morphologies and structural features of Co_3O_4, $MgCo_2O_4$ and MgO samples with different magnifications were investigated by a scanning electron microscope as shown in Figure 2. Co_3O_4 catalyst presents a microsphere-like morphology composed of smallest and smaller grain size with the average diameter of approximately 20–30 nm (Figure 2a,b). Smaller microspheres are derived from aggregation of fine grains of Co_3O_4. Upon Co substitution by Mg in the matrix of Co_3O_4, the morphology of the obtained $MgCo_2O_4$ turned into more uniform and smaller particles which exhibit the needle-shape morphology with the average size of about 10–20 nm (Figure 2c,d). A close overview of the magnified image of $MgCo_2O_4$ (Figure 2d) shows that the arrangement of particles displayed many intrinsic small holes/pores. The insertion of Mg has modified the morphology of the Co_3O_4 sample and greatly decreased the grain size, offering more apparent porosity of the catalyst surface. The observed morphology is proposed to play a determinant role in the catalytic oxidation process. Figure 2e,f show SEM image of MgO, with irregular and ununiform particles aggregated together. From Figure 2f, it is comprehensibly shown that narrow particles are agglutinated together and generate irregular particles of different size (35–45 nm) and shape.

Table 1. Summary of size, specific surface area, activation energy and results of peaks-fittings of O 1s binding energies and relative atomic percentage for Co_3O_4, $MgCo_2O_4$, and MgO. The corresponding ratios of $O_{Ads.}$ and $O_{Lat.}$ are presented in the last column.

Samples	PS (nm)	S_{BET} ($m^2 \cdot g^{-1}$)	Ea (kJ/mol)	Co^{3+}/Co^{2+} (%)	$O_{Lat.}$ (Co-O/Mg-O/Co-O-Mg)		$O_{Ads.}$(-OH)		$O_{Ads.}$(-CO_3^{2-})		$O_{Ads.}/O_{Lat.}$ (%)
					(At%)	BE (eV)	(At%)	BE (eV)	(At%)	BE (eV)	
Co_3O_4	30	48	68.9	0.45	68.85	529.38	31.15	531.37	-		0.45
$MgCo_2O_4$	22	82	38.5	0.54	37.25	529.41	44.70	531.40	18.05	532.29	1.68
MgO	45	15	-	-	98.05	529.72	1.95	531.32	-		0.02

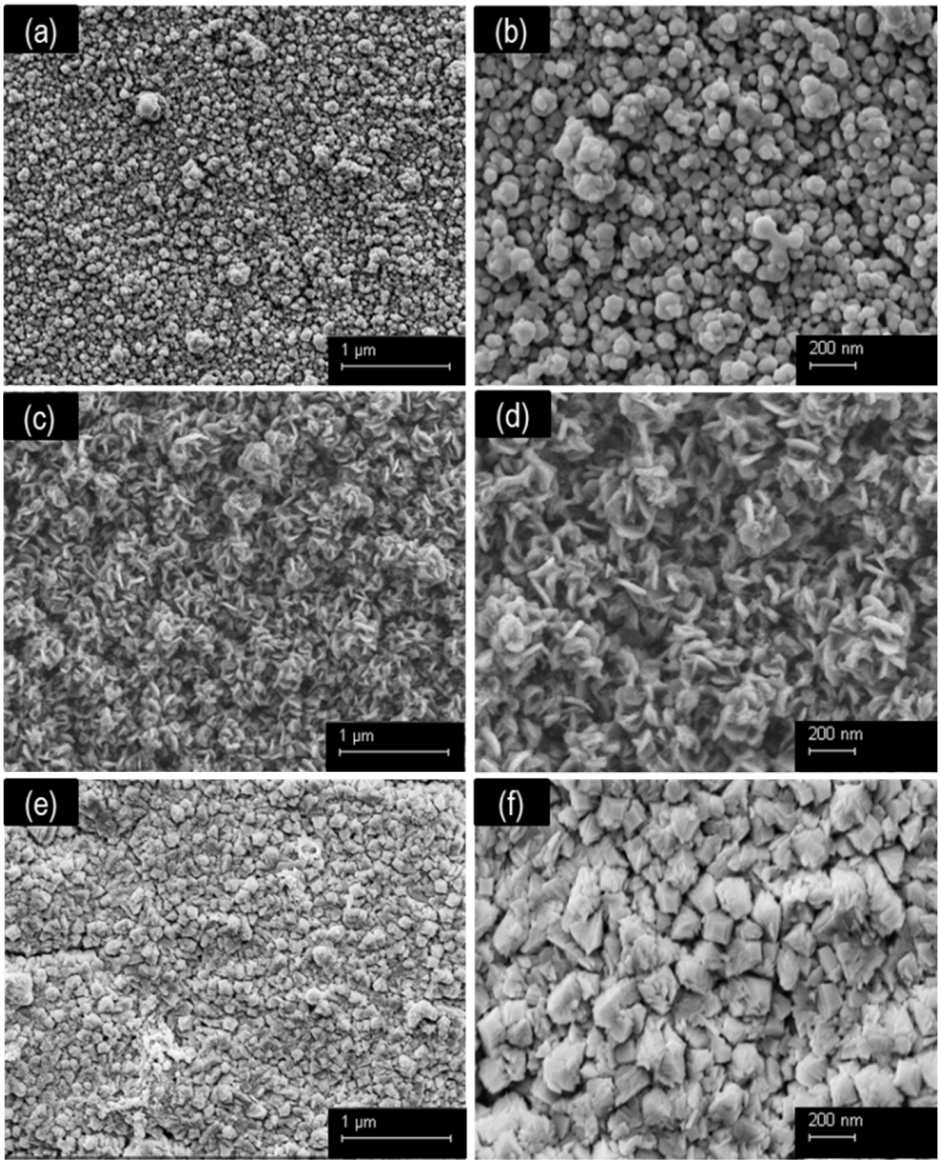

Figure 2. SEM micrographs of (**a**,**b**) Co_3O_4, $MgCo_2O_4$ (**c**,**d**) and (**e**,**f**) MgO obtained by co-precipitation.

2.3. Elemental Composition and Ionic States

In order to understand elemental contains and oxidation states as well as surface energy state distribution of the as-synthesized materials, EDS (see Figure S1 and Table S1) and XPS analysis were carried out. The results reveal the existence of Co 2p, Mg 1s, Mg 2p, and O 1s as depicted in Figure 3. As presented in Figure 3a, the Co 2p XPS spectrum and the two prominent peaks located at binding energies (BE) of 780.6 and 796.7 eV are ascribed to the Co $2p_{3/2}$ and Co $2p_{1/2}$, respectively, in close agreement with the literature [48,49]. The Gaussian fitting results shows two peaks that could be split up into two spin–orbit doublets, insinuating the coexistence of Co^{2+} and Co^{3+} in the matrix of $MgCo_2O_4$. The peaks centered at 780.01 and 796.7 eV are associated with Co^{3+} whereas the peaks at located 781.1 and 795.9 eV are assigned Co^{2+} species in $MgCo_2O_4$ (Figure 3a) [49,50]. In addition, the signals at 786.02 and 802.9 eV were assigned to satellite peaks. As for Co_3O_4 the Gaussian fitting results like in the above mentioned case shows that the Co 2p spectrum presents asymmetric peaks, with a notable shift towards to higher BE and which is consisted of several overlapping features emerging from $2p_{3/2}$ (783.3 eV) and $2p_{1/2}$ (796.5 eV) peaks assigned to Co^{2+} and Co^{3+} but without associated satellite signals [51]. The high resolution of Mg 1s core shell presented in Figure 3b display a weak peak located at ~1303.5 eV, putting

forward the occurrence of Mg^{2+} in the $MgCo_2O_4$ in good agreement with previous reported data [44]. As shown in Figure 3c, the Mg 2p spectrum show two peaks at ~52 eV, which deconvoluted displayed two distinct peaks at the binding energy of 51.50 and 50.20 eV assigned for Mg^{2+} and Mg^0, respectively, which proves the presence of the Mg element in the MgO structure according to previous reports [52,53].

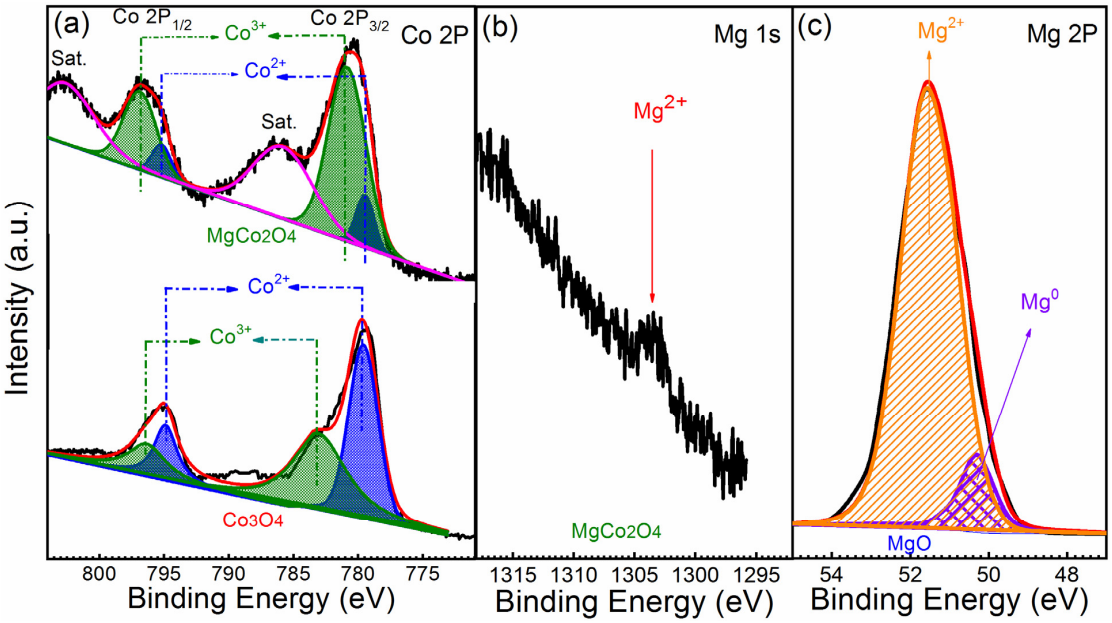

Figure 3. XPS spectra of (**a**) Co 2p, (**b**) Mg 1s, and (**c**) Mg 2P regions for the samples obtained by co-precipitation method.

Furthermore, high-resolution XPS spectra of O 1s were performed as presented in Figure 4. O 1s spectra have been deconvoluted into two and three curves for Co_3O_4 and $MgCo_2O_4$, respectively, with binding energies at 529.5, 531.2 and 532.3 eV. The most intense signal located at 529.5 eV is assigned to lattice oxygen ($O_{Lat.}$) in the metal (Mg/Co)-oxygen framework, or O^{2-} in surface Ov and adsorbed oxygen ($O_{Ads.}$), respectively [54]. The peaks at 531.2 and 532.3 eV are assigned to hydroxyl (OH^-) groups and some oxygenated species weakly bonded at the catalyst surface, respectively [55]. O1s patterns exhibit different profile for MgO, Co_3O_4, and $MgCo_2O_4$. As for $MgCo_2O_4$, for which the peaks of $O_{Ads.}$ were most intense than that of the $O_{Lat.}$, a completely different profile was shown. The proportions of oxygenated species detected at the surface of the catalyst were estimated and their ratio ($O_{Lat.}/O_{Ads.}$) are summarized in Table 1. It is well known that the $O_{Ads.}/O_{Lat.}$ ratio on the catalysts surface attest to the presence of more active Ov species [56]. In the present work, the highest $O_{Ads.}/O_{Lat.}$ ratio of 1.68 is obtained for the $MgCo_2O_4$ catalyst, while those of Co_3O_4 (0.45) and MgO (0.02) were notably lower. Obviously, $MgCo_2O_4$ exhibit the largest content of $O_{Ads.}$. It is well established that the occurrence of electrophilic oxygen species (O_2^{2-}/O^-) at the surface of TMOs catalysts enable facile generation of reactive radicals that could increase the oxidation reaction rate and allowed the enhancement of the catalytic process [57,58]. Therefore, the great amount of Co^{2+} and prolific electrophilic oxygen (O_2^{2-} and O^-) species will contribute to the high catalytic performance of the Mg-Co oxide samples.

2.4. Formation of Vacant Oxygen Species

In order to study the formation of vacant oxygen species we performed ab initio molecular dynamic simulations of toluene on the hydroxylated Co_3O_4 and $MgCo_2O_4$ (111) surfaces at 277 °C. For a fundamental understanding of vacancy formation mechanism, we have chosen the low index (111) surfaces as recent studies have shown that the synthesis by co-precipitation of cobalt based spinel lead to hexagonal particles, which mainly expose the

(111) [59]. For Co_3O_4, the lattice parameter (a = 8.09 Å) was taken from a previous work [60] while for $MgCo_2O_4$ the calculation of the lattice parameters values was performed in the present work and was found to be 8.18 Å. This value agrees well with the experimental value of a = 8.11Å taken from the work of Yagi et al. [61] These surfaces are known to be hydroxylated under most water-containing reactive environments. This is supported by ab initio thermodynamics predictions [62] as well as experimental observations [59,63]. On the (111) surface are two different types of oxygen in the topmost layer, one is saturated with four bonds to cobalt or magnesium ions and another type with three bonds to the metal ions and one dangling bond (see Fig.ESI2). When in contact with water, this dangling bond becomes saturated by accepting a proton and therefore on the hydroxylated surface both types of oxygen are saturated. In our simulations we only observe the oxygen atoms with four metal ions neighbors to form vacant oxygen species, by becoming pushed up, out of the slab (Figure 5). A highly unsaturated (reactive) oxygen that bridges two metal ions on the surface forms, leaving an oxygen vacancy in the slab. Supposedly this vacancy can be filled by an oxygen molecule to repeat the formation of a reactive oxygen species. Thus, the catalysis cycle would follow an intrafacial process of Mars–van Krevelen.

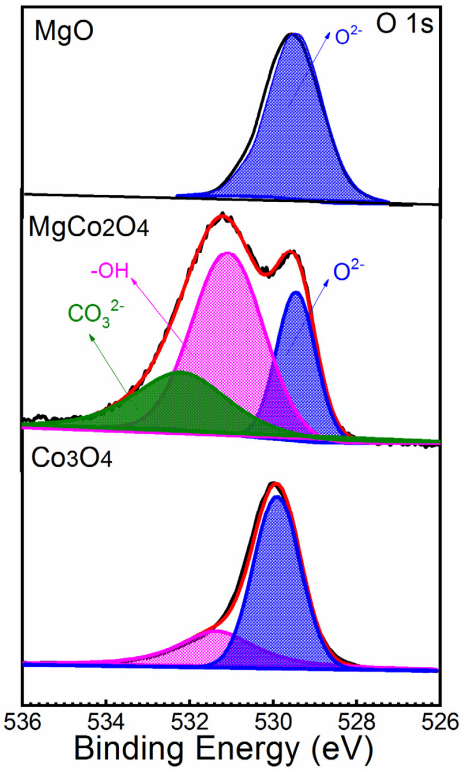

Figure 4. XPS spectra of O 1s regions for the samples prepared by co-precipitation method.

2.5. Reducibility

H_2-TPR is well known as an ideal technique to investigate the reducibility of catalysts. This analysis was performed, and results are presented in Figure 6. The pattern of MgO presents a major peak at ~720 °C and reveals that the framework of MgO is reduced at high temperature (700~760 °C) under H_2 atmosphere. In contrary, two prominent reduction peaks of spinel Co_3O_4 and $MgCo_2O_4$ are identified. Prominent peaks for Co_3O_4 sample located at ~390 and ~485 °C, correspond to the reduction of cobalt ions from Co^{3+} to Co^{2+} and Co^{2+} to Co^0, respectively [64,65]. However, it is obviously observed that the reduction peaks (Co^{3+} to Co^{2+}) and (Co^{2+} to Co^0) for $MgCo_2O_4$ are shifted to lower temperatures 379 and 455 °C, in good agreement with previous reported studies [66]. The observed changes revealed that Mg insertion in the matrix of Co_3O_4 easily enhanced the extraction of the surface $O_{Lat.}$ species, weakened the Co−O-Mg bond. It is noteworthy that the decrease of cobalt cation peaks for

$MgCo_2O_4$ sample toward low temperatures indicates that the reduction process is easier. One can thus suggest that the migration of $O_{Lat.}$ species from the bulk to the surface of $MgCo_2O_4$ samples at relatively low temperature is a consequence of their facile activation. [67,68] and that may lead to its higher catalytic activity than Co_3O_4 and MgO oxides.

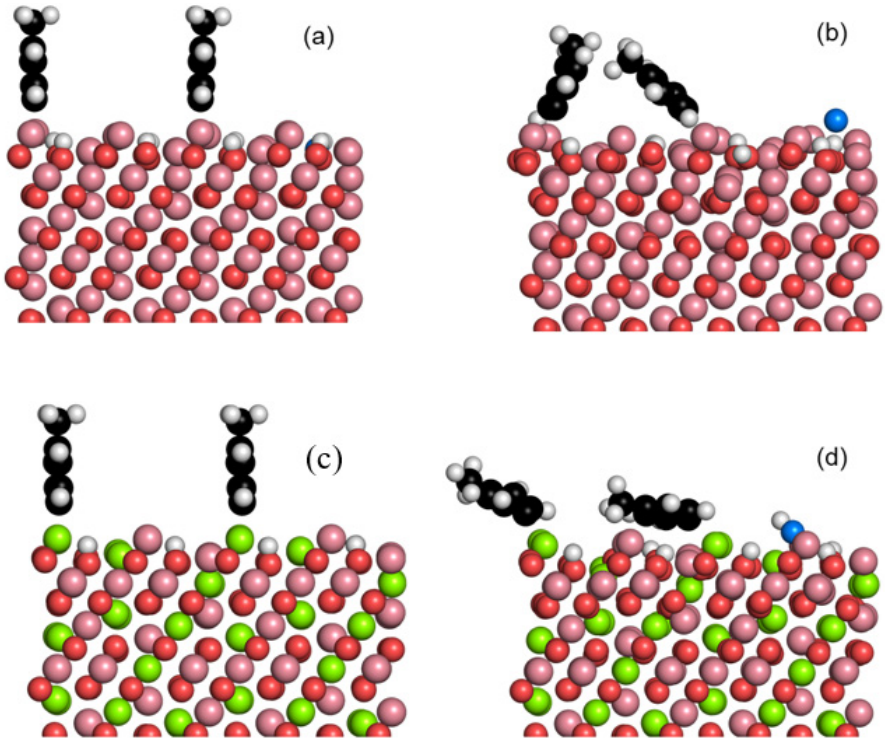

Figure 5. Snapshots of initial and final (10 ps) configurations of toluene adsorbed on hydroxylated Co_3O_4 (111) (**a**,**b**) and $MgCo_2O_4$ (111) (**c**,**d**) surfaces. Mg: green, Co: pink, slab oxygens: red, vacant oxygen: blue, carbon: black, hydrogen: white.

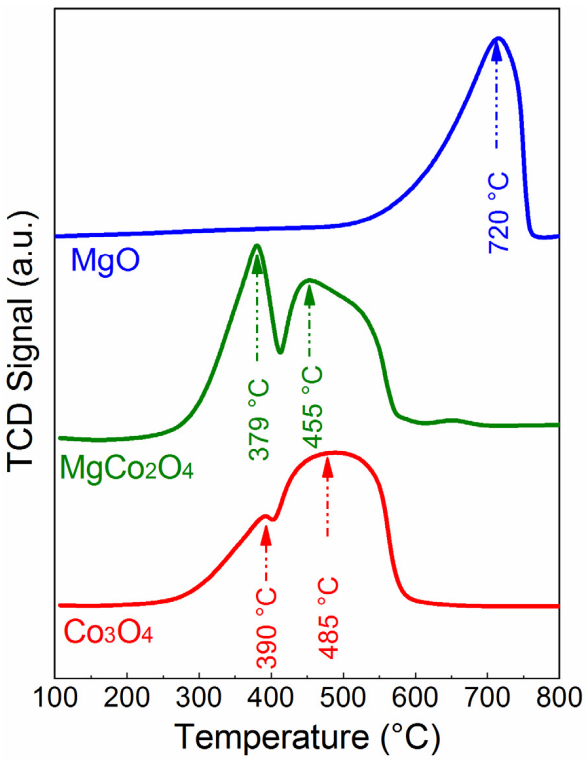

Figure 6. H_2-TPR profiles of Co_3O_4, $MgCo_2O_4$ and MgO catalysts.

2.6. Catalytic Test

2.6.1. Catalytic Activity

The measurement of toluene oxidation was performed within the temperature range of 100–400 °C (see Figure 7a) to evaluate the catalytic performance of each sample. Figure 7a displays the temperature dependence of the toluene conversion with samples, and the toluene conversion rises upon an increase of the reaction temperature. The performance variation of the catalysts is not obvious under 200 °C; however, a great difference was observed in terms of the temperature at which the final total oxidation was achieved. Then, toluene was gradually, easily and rapidly degraded over $MgCo_2O_4$ and Co_3O_4 as the reaction temperature was increased. The spinel $MgCo_2O_4$ sample, which reaches 50, 90 and 100% conversion to CO_2 and H_2O at ~242, ~250 and ~255 °C, respectively, exhibits higher catalytic performance compared to those of single-metal oxides (Co_3O_4 and MgO). MgO with only 20% conversion at ~377 °C shows the weak performance among the catalysts tested. Conversely, the performance of single Co_3O_4 with T_{100} = ~315 °C is ~122 °C lower than that that of $MgCo_2O_4$ (T_{100} = ~255 °C) for which a significant shift of T_{100} toward the low reaction temperature was observed. From the catalytic activity test, it is obvious that the performance of the $MgCo_2O_4$ sample in the deep oxidation of toluene is enhanced by substitution of Co by Mg species in the matrix of Co_3O_4, which is responsible of the shift of the reactions temperatures towards the lower values. The following performance order was observed: $MgCo_2O_4$ > Co_3O_4 > MgO and satisfactory confirmed that the presence of Mg species can substantially and remarkably enhance the performance of the Mg-Co oxides catalyst.

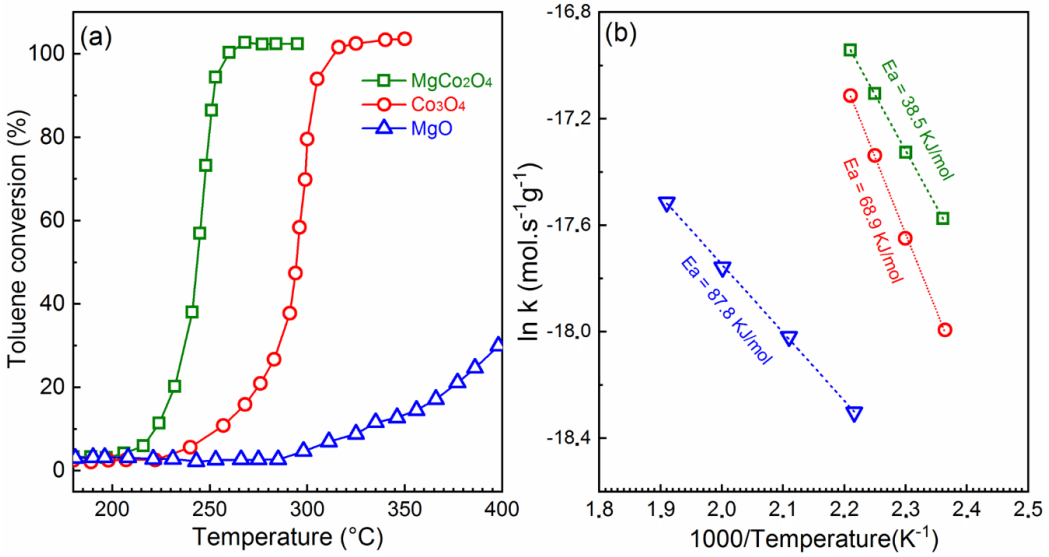

Figure 7. (**a**) Light-off curves and (**b**) Arrhenius plots of toluene reaction rates over spinel ($MgCo_2O_4$, Co_3O_4) and MgO catalysts.

In order to better assess their performances, active samples ($MgCo_2O_4$ and Co_3O_4) in this work, was compared with other Co-based oxides, perovskite, spinel, and noble metal catalysts from earlier published works and the results are displayed in table ESI2. The analysis of the results in table ESM1 indicated that $MgCo_2O_4$ still exhibits a comparable catalytic performance under the seemingly similar test conditions.

The apparent activation energies (Ea) were evaluated and shown in Figure 7b while the calculated data are presented in Table 1. Compared with the single-metal oxide Co_3O_4 (E_a = 68.9 kJ/mol), binary-metal oxides with a spinel $MgCo_2O_4$ structure exhibits the lowest apparent Ea (E_a = 38.5 kJ/mol). The lowest Ea implies the easiest toluene oxidation process over the $MgCo_2O_4$ samples. The result is in a total agreement with that of toluene conversion. From the above presented results, it is obvious that $MgCo_2O_4$ compared with Co_3O_4 possesses some outstanding properties that can be explained relying on the physico-

chemical properties of the catalysts above. The phase and structure analysis by XRD display broader peaks of $MgCo_2O_4$, implying smallest grains sized, and largest specific surface area which are favorable to toluene oxidation in close agreement with earlier reported works [69]. The microstructure and morphology study by SEM shows surface catalyst with several intrinsic small holes offering more apparent porosity, and suggesting the occurrence of more surface defect sites that is beneficial in the catalytic reaction process [70]. In addition to other physico-chemical analysis, XPS results revealed the highest ratio of Co^{3+}/Co^{2+} and $O_{Ads.}/O_{Lat.}$ for the $MgCo_2O_4$ sample. It has been earlier established that the excellent performance of Co-based oxide catalyst is strongly assigned to the presence at their surface of more Co^{2+} population and large quantity of oxygenated species. In fact, previous investigation certified that the preponderance of Co^{2+} facilitates the total conversion of toluene over Co-based oxide materials [71,72]. More importantly, the H_2-TPR profile (Figure 6) exhibited the best reducibility for $MgCo_2O_4$ sample, which is consistent with its performance towards toluene oxidation [73].

2.6.2. Long-Term Durability of $MgCo_2O_4$

The durability also known as long-term stability and the reproducibility test are among the key catalysts criteria required for an industrial application. In the present work, both tests were performed and are displayed on Figure 8. To investigate the catalytic stability, the time-on-stream (TOS) reaction was performed at ~260 °C, the temperature at which the toluene conversion over $MgCo_2O_4$ was ~100%. From Figure 8a, it is observed that, oxidation process of toluene over $MgCo_2O_4$ begin at ~99% conversion, and was kept almost constant within the first 10 h at ~260 °C, then shifted up to ~95.36% which is equivalent to a loss of ~4.38% conversion in long-term TOS after 30 h. The results of stability check attest that the $MgCo_2O_4$ spinel is stable and durable under a continuous supply of toluene and no deactivation was observed. The observed slide decrease of ~4.38% conversion from the first 10 h up to the 30rd hours is suggested to be a consequence of the coverage of actives sites at the surface of $MgCo_2O_4$ by soot particles and some other reactions products from the oxidation reaction process as well as competition of H_2O and oxygen adsorption on the active surface. Moreover, the stability/durability, the reproducibility test well known as a critical parameter for catalyst was performed. With this test, we wanted to test $MgCo_2O_4$ susceptibility to experience thermal deactivation which will usually accounts for their limited application in industrial field. $MgCo_2O_4$ exhibits excellent toluene conversion in fourth consecutive repeated runs (Figure 8b) attesting of its good reproducibility. Therefore, $MgCo_2O_4$ considered as an excellent binary oxide material for toluene deep oxidation with a promising catalytic application.

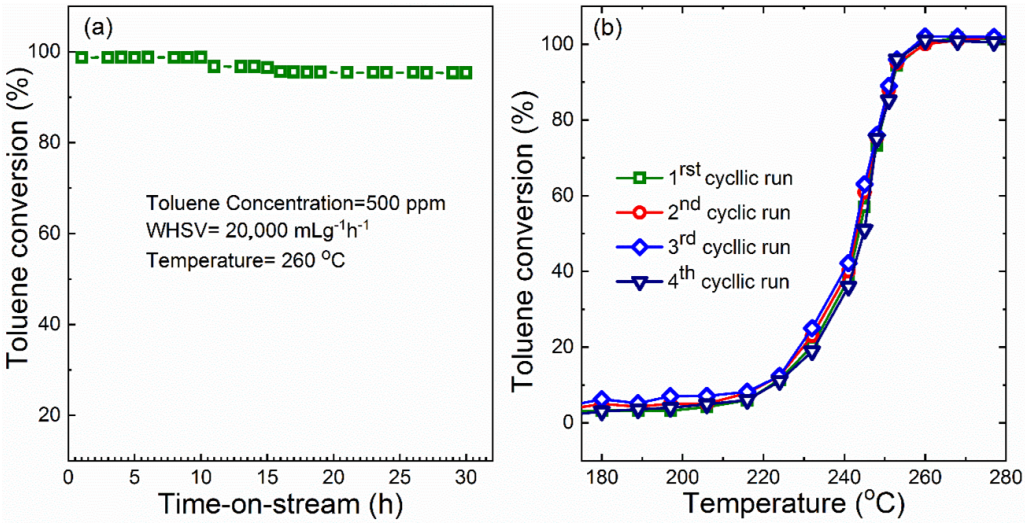

Figure 8. (a) Evolution of the catalytic long-term durability and (**b**) stability of toluene oxidation with time-on-stream over the $MgCo_2O_4$ catalyst at 300 °C (GHSV = 20,000 mL g^{-1} h^{-1}).

3. Experimental

3.1. Catalyst Preparation

The synthesis approach applied herein is an adapted version of a previously reported co-precipitation method [50,74,75]. All chemicals were provided by Sigma-Aldrich Pty Ltd., Hamburg, Germany. For MgO and Co_3O_4 synthesis, 1 mM of Magnesium acetylacetonate [$Mg(acac)_2$] and 1 mM of cobalt acetylacetonate [$Co(acac)_2$] were used as precursor and were separately dissolved in 200 mL of ethanol, respectively, then a solution of NaOH (2 M) was added in each solution dropwise under vigorous magnetically stirring until the pH value of ca. 10. The obtained phase was maintained under vigorous stirring for 3 h at a constant temperature of ~60 °C. Then, the deionized H_2O was used to wash the obtained precipitate until pH equivalent to ~7. Finally, the solid obtained was overnight at ~100 °C followed by an annealing in an electric furnace in static air at ~500 °C for 3 h. As for Mg-Co binary oxide is concerned, 1mM of $Co(acac)_2$ and 0.5 mM $Mg(acac)_2$ were dissolved in 200 mL of ethanol. Then, NaOH (2 M) solution was added dropwise into the precursor solution at room temperature until the pH~10. The same procedure adopted for the preparation of single oxide was followed. The catalyst sample thus obtained was labelled $MgCo_xO_4$, where x ($0 < x < 2$) represents the nominal element ratio of Mg to Co used in the synthesis process.

3.2. Catalyst Characterization

The Brunauer–Emmett–Teller (BET) surface specific area of each sample was measured on a nitrogen physisorption apparatus (NOVA3000, Quantachrome) and estimated throughout BET equation. Before the measurement, the catalysts were degassed at 300 °C under vacuum for 3 h to evacuate H_2O and CO_2, then adsorbed by nitrogen at ~196 °C and desorbed at room temperature. X-ray diffraction (XRD) analysis of the as-prepared single (MgO, Co_3O_4) and mixed ($MgCo_2O_4$) oxides were performed, using Cu Kα (λ = 0.154056 nm) radiation from Bruker (D8 Focus at 40 kV and 150 mA). The resulting crystalline phases were in excellent agreement with the Joint Committee on Powder Diffraction Standards (JCPDS) database. The samples were scanned within the 2θ range of 20 to 80°. The surface morphology of MgO, Co_3O_4 and $MgCo_2O_4$, was analyzed by an ultra-high-resolution scanning electron microscopy (SEM, S-4800 Hitachi). To determine the surface elemental composition and ionic states, X-ray photoelectron spectroscopy (XPS) were performed on an ULVAC PHI 5000 Versa Probe-II equipment (Japan). C 1s peak at 284 eV was used as reference for all electron binding energies. In order to investigate the formation of Ov species, ab initio molecular dynamic simulation of toluene on the hydroxylate Co_3O_4 and $MgCo_2O_4$ (111) was performed (see computational details in ESM). To investigate on the reducibility of the three set of catalyst, H_2-Temperature programmed reduction (H_2-TPR) analysis was investigated using a chemical adsorption equipment (PCA-1200, Beijing Builder) equipped with a quartz reactor and TCD detector. As annealing facilitates the formation of catalysts possessing the largest surface area and reducibility, prior to the test, 60 mg of each catalyst were firstly pre-treated for 40 min in an Ar flow within room temperature to ~400 °C and then followed by a cooling down to ~100 °C. The TPR analysis were carry out with samples exposed under a 5% H_2/Ar with a flowrate of 30 mL/min using a heating rate of 10 °C/min up to ~900 °C.

3.3. Catalytic Test

The performance of the as-prepared TMOs towards toluene total oxidation was evaluated in a tubular (internal diameter, 6 mm) fixed-bed reactor system made of stainless steel and 0.06 g (40–60 mesh) of the catalyst was placed at the center of the reactor. The reaction gas mixture was composed of 500 ppm toluene and 20% O_2/Ar, for a total flow of 75 mL/min, corresponding to a gas hourly space velocity (GHSV) of 20,000 mL g^{-1} h^{-1}. Toluene in the flow gas was generated continuously by the mean of an Ar bubbler through liquid toluene container and chilled at 0 °C in an isothermal bath composed of ice and water. To avoid toluene condensation on the reactor walls, the entire gas lines covered by a heating band was heated up to 100 °C. The inlet and outlet gas were detected online by

a flame ionization detector (FID) in a gas chromatograph (GC-6890A) equipped with a thermal conductivity detector (TCD). The toluene conversion ($X_{toluene}$) was estimated at different temperature according to the following equations:

$$(X_{toluene}) = ([X_{toluene}]in\text{-}([X_{toluene}]out) \times 100 \quad (1)$$

where $([X_{toluene}]_{in}$ and $([X_{toluene}]_{out}$ correspond to the reactants and products concentration of toluene. The apparent activation energies (E_a) were estimated for toluene total conversions to CO_2 and H_2O lower than 20%, using the following Arrhenius relationship:

$$K = A \exp(-E_a/RT) \quad (2)$$

where R is the gas constant (kJ mol^{-1} K^{-1}); T(K) is the reactor temperature; and A is the pre-exponential factor.

4. Conclusions

In summary, MgO, Co_3O_4 and $MgCo_2O_4$ metal oxides catalysts were prepared by co-precipitation approach and systematically analyzed in terms of structure (XRD), chemical composition and ionic states (XPS) and morphology. More importantly, the as-prepared samples were tested as catalyst toward total oxidation of toluene. The investigation of the long-term durability and stability of $MgCo_2O_4$ in the process of toluene conversion indicated that, the bimetallic catalyst exhibits the most outstanding catalytic activity. It is worth noting that the insertion of Mg in the matrix of Co_3O_4 played a key role on the physico-chemical properties of the as-synthesized binary oxide samples. Compared with single oxide (MgO, Co_3O_4) catalysts, the $MgCo_2O_4$ binary catalyst exhibits the largest specific surface area, the highest Co^{3+}/Co^{2+} and $O_{Ads.}/O_{Lat.}$ ratios as well as the interesting low-temperature reducibility. Therefore, Co_3O_4 modified by magnesium derived from the Co-precipitation approach is a viable and promising catalyst for toluene total conversion. The investigation has shown that, the structure and catalytic property $MgCo_2O_4$ can be successfully improved by a tailored control of Mg concentration in the final binary oxide.

Supplementary Materials: The following supporting information can be downloaded at: https://www.mdpi.com/article/10.3390/catal12040411/s1, Section S1: Figure S1: EDS pattern of MgCo2O4; Table S1: EDS bulk elemental analysis of MgCo2O4. Section S2: computational details; Figure S2: Top views of: (a) Co3O4(111) and (b) MgCo2O4(111) surfaces. Mg: green, Co: pink, slab oxygens: red, unsaturated slab oxygen with only 3 metal ions neighbors: cyan. Section S3: Table S2: Catalytic performance and test conditions of toluene over $MgCo_2O_4$, Co_3O_4 and other related catalysts earlier reported in the literature. References [76–79] are cited in the supplementary materials.

Author Contributions: A.A.Z.: Investigation, Writing—original draft. D.M. and D.M.D.: Data curation. H.T.A.: Data curation. T.K.: Investigation, Formal analysis. S.K.: Methodology, Writing—reviewing & editing, Funding acquisition. I.N.N.: Validation. P.M.K.: Conceptualization, Funding acquisition, Methodology, Project administration, Supervision, Writing—review and editing. All authors have read and agreed to the published version of the manuscript.

Funding: This research was funded by the Deutsche Forschungsgemeinschaft (DFG, German Research Foundation) (Grant 388390466—TRR 247) and the Deutscher Akademischer Austauschdienst (DAAD) (Grant No. ST16-04.12.2020).

Acknowledgments: S.K. and T.K. acknowledge computing time granted by the Center for Computational Sciences and Simulation (CCSS) of the Universität of Duisburg-Essen and provided on the supercomputer magnitude (DFG grants INST 20876/209-1 FUGG, INST 20876/243-1 FUGG) at the Zentrum für Informations- und Mediendienste (ZIM). S.K. gratefully acknowledge the Deutsche Forschungsgemeinschaft (DFG, German Research Foundation) for the funding 388390466—TRR 247. P.M.K. kindly acknowledge the Deutscher Akademischer Austauschdienst (DAAD) for the financial support.

Conflicts of Interest: There is no conflict of interest to declare.

References

1. Kim, S.C.; Park, Y.-K.; Nah, J.W. Property of a highly active bimetallic catalyst based on a supported manganese oxide for the complete oxidation of toluene. *Powder Technol.* **2014**, *266*, 292–298. [CrossRef]
2. Cheng, Y.; Gao, X.; Zhang, X.; Su, J.; Wang, G.; Wang, L. Synthesis of a TiO_2–Cu_2O composite catalyst with enhanced visible light photocatalytic activity for gas-phase toluene. *New J. Chem.* **2018**, *42*, 9252–9259. [CrossRef]
3. Rokicinska, A.; Zurowska, M.; Latka, P.; Drozdek, M.; Michalik, M.; Kustrowski, P. Design of Co_3O_4@SiO_2 Nanorattles for Catalytic Toluene Combustion based on Bottom-Up Strategy Involving Spherical Poly(styrene-co-acrylic Acid) Template. *Catalyst* **2021**, *11*, 1097. [CrossRef]
4. Zhang, X.; Yang, Y.; Song, L.; Chen, J.; Yang, Y.; Wang, Y. Enhanced adsorption performance of gaseous toluene on defective UiO-66 metal organic framework: Equilibrium and kinetic studies. *J. Hazard. Mater.* **2018**, *365*, 597–605. [CrossRef]
5. Wu, X.; Han, R.; Liu, Q.; Su, Y.; Lu, S.; Yang, L.; Song, C.; Ji, N.; Ma, D.; Lu, X. A review of confined-structure catalysts in the catalytic oxidation of VOCs: Synthesis, characterization, and applications. *Catal. Sci. Technol.* **2021**, *11*, 5374–5387. [CrossRef]
6. Delimaris, D.; Ioannides, T. VOC oxidation over CuO–CeO_2 catalysts prepared by a combustion method. *Appl. Catal. B: Environ.* **2009**, *89*, 295–302. [CrossRef]
7. Wang, F.; Dai, H.; Deng, J.; Bai, G.; Ji, K.; Liu, Y. Manganese Oxides with Rod-, Wire-, Tube-, and Flower-Like Morphologies: Highly Effective Catalysts for the Removal of Toluene. *Environ. Sci. Technol.* **2012**, *46*, 4034–4041. [CrossRef]
8. Jiang, Z.; He, C.; Dummer, N.F.; Shi, J.; Tian, M.; Ma, C.; Hao, Z.; Taylor, S.H.; Ma, M.; Shen, Z. Insight into the Efficient Oxidation of Methyl-Ethyl-Ketone over Hierarchically Micro-Mesostructured Pt/K-(Al)SiO_2 Nanorod Catalysts: Structure-Activity Relationships and Mechanism. *Appl. Catal. B Environ.* **2018**, *226*, 220–233. [CrossRef]
9. Wang, H.; Yang, W.; Tian, P.; Zhou, J.; Tang, R.; Wu, S. A Highly Active and Anti-Coking Pd-Pt/SiO_2 Catalyst for Catalytic Combustion of Toluene at Low Temperature. *Appl. Catal. A Gen.* **2017**, *529*, 60–67. [CrossRef]
10. Kim, S.C. The catalytic oxidation of aromatic hydrocarbons over supported metal oxide. *J. Hazard. Mater.* **2002**, *91*, 285–299. [CrossRef]
11. Kim, S.C.; Shim, W.G. Catalytic combustion of VOCs over a series of manganese oxide catalysts. *Appl. Catal. B Environ.* **2010**, *98*, 180–185. [CrossRef]
12. Grimaud, A.; Diaz-Morales, O.; Han, B.; Hong, W.T.; Lee, Y.-L.; Giordano, L.; Stoerzinger, K.; Koper, M.T.M.; Shao-Horn, Y. Activating lattice oxygen redox reactions in metal oxides to catalyse oxygen evolution. *Nat. Chem.* **2017**, *9*, 457–465. [CrossRef] [PubMed]
13. Ma, M.; Huang, H.; Chen, C.; Zhu, Q.; Yue, L.; Albilali, R.; He, C. Highly active SBA-15-confined Pd catalyst with short rod-like micro-mesoporous hybrid nanostructure for n-butylamine low-temperature destruction. *Mol. Catal.* **2018**, *455*, 192–203. [CrossRef]
14. He, C.; Jiang, Z.; Ma, M.; Zhang, X.; Douthwaite, M.; Shi, J.-W.; Hao, Z. Understanding the Promotional Effect of Mn_2O_3 on Micro-/Mesoporous Hybrid Silica Nanocubic-Supported Pt Catalysts for the Low-Temperature Destruction of Methyl Ethyl Ketone: An Experimental and Theoretical Study. *ACS Catal.* **2018**, *8*, 4213–4229. [CrossRef]
15. Zhou, G.; Lan, H.; Gao, T.; Xie, H. Influence of Ce/Cu ratio on the performance of ordered mesoporous CeCu composite oxide catalysts. *Chem. Eng. J.* **2014**, *246*, 53–63. [CrossRef]
16. Bai, B.; Arandiyan, H.; Li, J. Comparison of the performance for oxidation of formaldehyde on nano-Co_3O_4, 2D-Co_3O_4, and 3D-Co_3O_4 catalysts. *Appl. Catal. B Environ.* **2013**, *142–143*, 677–683. [CrossRef]
17. Ren, Q.; Mo, S.; Peng, R.; Feng, Z.; Zhang, M.; Chen, L.; Fu, M.; Wu, J.; Ye, D. Controllable synthesis of 3D hierarchical Co_3O_4 nanocatalysts with various morphologies for the catalytic oxidation of toluene. *J. Mater. Chem. A* **2017**, *6*, 498–509. [CrossRef]
18. Liao, Y.; He, L.; Man, C.; Chen, L.; Fu, M.; Wu, J.; Ye, D.; Huang, B. Diameter-dependent catalytic activity of ceria nanorods with various aspect ratios for toluene oxidation. *Chem. Eng. J.* **2014**, *256*, 439–447. [CrossRef]
19. Zhou, K.; Wang, X.; Sun, X.; Peng, Q.; Li, Y. Enhanced catalytic activity of ceria nanorods from well-defined reactive crystal planes. *J. Catal.* **2005**, *229*, 206–212. [CrossRef]
20. Piumetti, M.; Fino, D.; Russo, N. Mesoporous manganese oxides prepared by solution combustion synthesis as catalysts for the total oxidation of VOCs. *Appl. Catal. B Environ.* **2014**, *163*, 277–287. [CrossRef]
21. Xie, Y.; Yu, Y.; Gong, X.; Guo, Y.; Guo, Y.; Wang, Y.; Lu, G. Effect of the crystal plane figure on the catalytic performance of MnO_2 for the total oxidation of propane. *CrystEngComm* **2015**, *17*, 3005–3014. [CrossRef]
22. Huang, X.; Peng, Y.; Liu, X.; Li, K.; Deng, Y.; Li, J. The Promotional Effect of MoO_3 Doped V_2O_5/TiO_2 for Chlorobenzene Oxidation. *Catal. Commun.* **2015**, *69*, 161–164. [CrossRef]
23. Dai, Q.; Yin, L.-L.; Bai, S.; Wang, W.; Wang, X.; Gong, X.-Q.; Lu, G. Catalytic Total Oxidation of 1,2-Dichloroethane over VOx/CeO_2 Catalysts: Further Insights via Isotopic Tracer Techniques. *Appl. Catal. B Environ.* **2016**, *182*, 598–610. [CrossRef]
24. Zhang, C.; Zhang, Z.; Sui, C.; Yuan, F.; Niu, X.; Zhu, Y. Catalytic Decomposition of N_2O over Co–Ti Oxide Catalysts: Inter-action between Co and Ti Oxide. *ChemCatChem* **2016**, *8*, 2155–2164. [CrossRef]
25. Perez-Ramirez, J.; Kapteijn, F.; Schöffel, K.; Moulijn, J.A. Formation and control of N_2O in nitric acid production—Where do we stand today? *Appl. Catal. B Environ.* **2003**, *44*, 117–151. [CrossRef]
26. Stelmachowski, P.; Maniak, G.; Kaczmarczyk, J.; Zasada, F.; Piskorz, W.; Kotarba, A.; Sojka, Z. Mg and Al substituted cobalt spinels as catalysts for low temperature deN_2O—Evidence for octahedral cobalt active sites. *Appl. Catal. B Environ.* **2014**, *146*, 105–111. [CrossRef]

27. Wei, X.; Wang, Y.; Li, X.; Wu, R.; Zhao, Y. Co3O4 supported on bone-derived hydroxyapatite as potential catalysts for N_2O catalytic decomposition. *Mol. Catal.* **2020**, *491*, 111005. [CrossRef]
28. Zasada, F.; Piskorz, W.; Janas, J.; Gryboś, J.; Indyka, P.; Sojka, Z. Reactive Oxygen Species on the (100) Facet of Cobalt Spinel Nanocatalyst and Their Relevance in $^{16}O_2/^{18}O_2$ Isotopic Exchange, DeN_2O, and DeCH_4 Processes—A Theoretical and Experimental Account. *ACS Catal.* **2015**, *5*, 6879–6892. [CrossRef]
29. Kaczmarczyk, J.; Zasada, F.; Janas, J.; Indyka, P.; Piskorz, W.; Kotarba, A.; Sojka, Z. Thermodynamic Stability, Redox Properties, and Reactivity of Mn_3O_4, Fe_3O_4, and Co_3O_4 Model Catalysts for N2O Decomposition: Resolving the Origins of Steady Turnover. *ACS Catal.* **2016**, *6*, 1235–1246. [CrossRef]
30. Zasada, F.; Gryboś, J.; Budiyanto, E.; Janas, J.; Sojka, Z. Oxygen species stabilized on the cobalt spinel nano-octahedra at various reaction conditions and their role in catalytic CO and CH_4 oxidation, N_2O decomposition and oxygen isotopic exchange. *J. Catal.* **2019**, *371*, 224–235. [CrossRef]
31. Kouotou, P.M.; Waqas, M.; El Kasmi, A.; Atour, Z.; Tian, Z.-Y. Influence of Co addition on Ni-Co mixed oxide catalysts toward the deep oxidation of low-rank unsaturated hydrocarbons. *Appl. Catal. A Gen.* **2021**, *612*, 117990. [CrossRef]
32. Tian, Z.Y.; Vieker, H.; Kouotou, P.M.; Beyer, A. In situ characterization of Cu–Co oxides for catalytic application. *Faraday Discuss.* **2015**, *177*, 249–262. [CrossRef] [PubMed]
33. Kouotou, P.M.; Vieker, H.; Tian, Z.Y.; Ngamou, P.H.T.; Kasmi, A.E.; Beyer, A.; Gölzhäuser, A.; Kohse-Höinghaus, K. Structure–Activity Relation of Spinel-Type Co–Fe Oxides for Low-Temperature CO Oxidation. *Catal. Sci. Technol.* **2014**, *4*, 3359–3367. [CrossRef]
34. Xue, L.; Zhang, C.; He, H.; Teraoka, Y. Catalytic decomposition of N_2O over CeO_2 promoted Co_3O_4 spinel catalyst. *Appl. Catal. B Environ.* **2007**, *75*, 167–174. [CrossRef]
35. Zhang, Q.; Tang, X.; Ning, P.; Duan, Y.; Song, Z.; Shi, Y. Enhancement of N_2O catalytic decomposition over Ca modified Co_3O_4 catalyst. *RSC Adv.* **2015**, *5*, 51263–51270. [CrossRef]
36. Li, Y.; Tang, F.; Wang, D.; Wang, X. A Key Step for Preparing Highly Active Mg–Co Composite Oxide Catalysts for N_2O Decomposition. *Catal. Sci. Technol.* **2021**, *11*, 3737–3745. [CrossRef]
37. Maniak, G.; Stelmachowski, P.; Kotarba, A.; Sojka, Z.; Rico-Pérez, V.; Bueno-López, A. Rationales for the Selection of the Best Precursor for Potassium Doping of Cobalt Spinel Based DeN_2O Catalyst. *Appl. Catal. B Environ.* **2013**, *136–137*, 302–307. [CrossRef]
38. Gölden, V.; Sokolov, S.; Kondratenko, V.A.; Kondratenko, E.V. Effect of the Preparation Method on High-Temperature de-N_2O Performance of Na–CaO Catalysts. A Mechanistic Study. *Appl. Catal. B Environ.* **2010**, *101*, 130–136. [CrossRef]
39. Ohnishi, C.; Asano, K.; Iwamoto, S.; Chikama, K.; Inoue, M. Alkali-doped Co_3O_4 catalysts for direct decomposition of N_2O in the presence of oxygen. *Catal. Today* **2007**, *120*, 145–150. [CrossRef]
40. Rezaei, M.; Khajenoori, M.; Nematollahi, B. Synthesis of high surface area nanocrystalline MgO by pluronic P123 triblock copolymer surfactant. *Powder Technol.* **2011**, *205*, 112–116. [CrossRef]
41. Chandar, N.K.; Jayavel, R. Synthesis and characterization of C14TAB passivated cerium oxide nanoparticles prepared by co-precipitation route. *Phys. E Low-Dimens. Syst. Nanostructures* **2014**, *58*, 48–51. [CrossRef]
42. Diachenko, O.; Opanasuyk, A.; Kurbatov, D.; Opanasuyk, N.; Kononov, O.; Nam, D.; Cheong, H. Surface Morphology, Structural and Optical Properties of MgO Films Obtained by Spray Pyrolysis Technique. *Acta Phys. Pol. A* **2016**, *130*, 805–810. [CrossRef]
43. Jadhav, H.S.; Roy, A.; Thorat, G.M.; Gil Seo, J. Facile and cost-effective growth of a highly efficient $MgCo_2O_4$ electrocatalyst for methanol oxidation. *Inorg. Chem. Front.* **2018**, *5*, 1115–1120. [CrossRef]
44. Chen, H.; Du, X.; Wu, R.; Wang, Y.; Sun, J.; Zhang, Y.; Xu, C. Facile hydrothermal synthesis of porous $MgCo_2O_4$ nanoflakes as an electrode material for high-performance asymmetric supercapacitors. *Nanoscale Adv.* **2020**, *2*, 3263–3275. [CrossRef]
45. Kitamura, N.; Tanabe, Y.; Ishida, N.; Idemoto, Y. The atomic structure of a $MgCo_2O_4$ nanoparticle for a positive electrode of a Mg rechargeable battery. *Chem. Commun.* **2019**, *55*, 2517–2520. [CrossRef] [PubMed]
46. Reddy, M.V.; Xu, Y.; Rajarajan, V.; Ouyang, T.; Chowdari, B.V.R. Template Free Facile Molten Synthesis and Energy Storage Studies on MCo_2O_4 (M = Mg, Mn) as Anode for Li-Ion Batteries. *ACS Sustain. Chem. Eng.* **2015**, *3*, 3035–3042. [CrossRef]
47. Zhang, C.; Guo, Y.; Guo, Y.; Lu, G.; Boreave, A.; Retailleau, L.; Baylet, A.; Giroir-Fendler, A. $LaMnO_3$ Perovskite Oxides Pre-pared by Different Methods for Catalytic Oxidation of Toluene. *Appl. Catal. B Environ.* **2014**, *148–149*, 490–498. [CrossRef]
48. Bao, F.; Wang, X.; Zhao, X.; Wang, Y.; Ji, Y.; Zhang, H.; Liu, X. Controlled growth of mesoporous $ZnCo_2O_4$ nanosheet arrays on Ni foam as high-rate electrodes for supercapacitors. *RSC Adv.* **2013**, *4*, 2393–2397. [CrossRef]
49. Gao, H.; Wang, X.; Wang, G.; Hao, C.; Huang, C.; Jiang, C. Facile Construction of a $MgCo_2O_4$@$NiMoO_4$/NF Core–Shell Nanocomposite for High-Performance Asymmetric Supercapacitors. *J. Mater. Chem. C* **2019**, *7*, 13267–13278. [CrossRef]
50. Zamudio, M.A.; Bensaid, S.S.; Fino, D.; Russo, N. Influence of the $MgCo_2O_4$ Preparation Method on N_2O Catalytic Decomposition. *Ind. Eng. Chem. Res.* **2011**, *50*, 2622–2627. [CrossRef]
51. Zhang, X.; Zhao, M.; Song, Z.; Zhao, H.; Liu, W.; Zhao, J.; Ma, Z.; Xing, Y. The effect of different metal oxides on the catalytic activity of a Co_3O_4 catalyst for toluene combustion: Importance of the structure–property relationship and surface active species. *New J. Chem.* **2019**, *43*, 10868–10877. [CrossRef]
52. Kim, M.; Yoo, J.; Kim, J. A p-nitroaniline redox-active solid-state electrolyte for battery-like electrochemical capacitive energy storage combined with an asymmetric supercapacitor based on metal oxide functionalized β-polytype porous silicon carbide electrodes. *Dalton Trans.* **2017**, *46*, 6588–6600. [CrossRef] [PubMed]

53. Huang, Z.; Wang, Z.; Zheng, X.; Guo, H.; Li, X.; Jing, Q.; Yang, Z. Effect of Mg doping on the structural and electrochemical performance of $LiNi_{0.6}Co_{0.2}Mn_{0.2}O_2$ cathode materials. *Electrochim. Acta* **2015**, *182*, 795–802. [CrossRef]
54. Jadhav, H.S.; Pawar, S.M.; Jadhav, A.H.; Thorat, G.M.; Seo, J.G. Hierarchical Mesoporous 3D Flower-like $CuCo_2O_4$/NF for High-Performance Electrochemical Energy Storage. *Sci. Rep.* **2016**, *6*, 31120. [CrossRef]
55. Lei, J.; Wang, S.; Li, J. Mesoporous Co_3O_4 Derived from Facile Calcination of Octahedral Co-MOFs for Toluene Catalytic Oxidation. *Ind. Eng. Chem. Res.* **2020**, *59*, 5583–5590. [CrossRef]
56. Wang, K.; Cao, Y.; Hu, J.; Li, Y.; Xie, J.; Jia, D. Solvent-Free Chemical Approach to Synthesize Various Morphological Co_3O_4 for CO Oxidation. *ACS Appl. Mater. Interfaces* **2017**, *9*, 16128–16137. [CrossRef]
57. Liu, B.; Li, C.; Zhang, G.; Yao, X.; Chuang, S.S.C.; Li, Z. Oxygen Vacancy Promoting Dimethyl Carbonate Synthesis from CO_2 and Methanol over Zr-Doped CeO_2 Nanorods. *ACS Catal.* **2018**, *8*, 10446–10456. [CrossRef]
58. Rousseau, S.; Loridant, S.; Delichere, P.; Boreave, A.; Deloume, J.P.; Vernoux, P. La(1−x)SrxCo1−yFeyO3 Perovskites Prepared by Sol–Gel Method: Characterization and Relationships with Catalytic Properties for Total Oxidation of Toluene. *Appl. Catal. B Environ.* **2009**, *88*, 438–447. [CrossRef]
59. Rabe, A.; Büker, J.; Salamon, S.; Koul, A.; Hageman, U.; Landers, J.; Ortega, F.K.; Peng, B.-X.; Muhlr, M.; Wende, H.; et al. The Roles of Composition and Meso-structure of Cobalt-Based Spinel Catalysts in Oxygen Evolution Reactions. *Chem. Eur. J.* **2021**, *27*, 17038–17048. [CrossRef]
60. Kox, T.; Spohr, E.; Kenmoe, S. Impact of Solvation on the Structure and Reactivity of the Co_3O_4 (001)/H_2O Interface: Insights from Molecular Dynamics Simulations. *Front. Energy Res.* **2020**, *8*, 312–321. [CrossRef]
61. Yagi, S.; Ichikawa, Y.; Yamada, I.; Doi, T.; Ichitsubo, T.; Matsubara, E. Synthesis of Binary Magnesium–Transition Metal Oxides via Inverse Coprecipitation. *Jpn. J. Appl. Phys.* **2013**, *52*, 25501. [CrossRef]
62. Yan, G.; Sautet, P. Surface Structure of Co_3O_4 (111) under Reactive Gas-Phase Environments. *ACS Catal.* **2019**, *9*, 6380–6392. [CrossRef]
63. Schwarz, M.; Faisal, F.; Mohr, S.; Hohner, C.; Werner, K.; Xu, T.; Skála, T.; Tsud, N.; Prince, K.C.; Matolín, V.; et al. Structure-Dependent Dissociation of Water on Cobalt Oxide. *J. Phys. Chem. Lett.* **2018**, *9*, 2763–2769. [CrossRef] [PubMed]
64. Liu, Y.; Dai, H.; Deng, J.; Xie, S.; Yang, H.; Tan, W.; Han, W.; Jiang, Y.; Guo, G. Mesoporous Co_3O_4-Supported Gold Nano-catalysts: Highly Active for the Oxidation of Carbon Monoxide, Benzene, Toluene, and o-Xylene. *J. Catal.* **2014**, *309*, 408–418. [CrossRef]
65. Ma, L.; Seo, C.Y.; Chen, X.; Sun, K.; Schwank, J.W. Indium-doped Co_3O_4 nanorods for catalytic oxidation of CO and C_3H_6 towards diesel exhaust. *Appl. Catal. B Environ.* **2018**, *222*, 44–58. [CrossRef]
66. Zheng, L.; Wu, C.-C.; Xu, X.-F. Catalytic decomposition of N_2O over Mg-Co and Mg-Mn-Co composite oxides. *J. Fuel Chem. Technol.* **2016**, *44*, 1494–1501. [CrossRef]
67. He, C.; Yu, Y.; Yue, L.; Qiao, N.; Li, J.; Shen, Q.; Yu, W.; Chen, T.; Hao, Z. Low-temperature removal of toluene and propanal over highly active mesoporous CuCeOx catalysts synthesized via a simple self-precipitation protocol. *Appl. Catal. B Environ.* **2014**, *147*, 156–166. [CrossRef]
68. Konsolakis, M.; Carabineiro, S.A.C.; Marnellos, G.E.; Asad, M.F.; Soares, O.S.G.P.; Pereira, M.F.R.; Órfão, J.J.M.; Figueiredo, J.L. Effect of Cobalt Loading on the Solid-State Properties and Ethyl Acetate Oxidation Performance of Cobalt-Cerium Mixed Oxides. *J. Colloid Interface Sci.* **2017**, *496*, 141–149. [CrossRef]
69. Chen, X.; Chen, X.; Yu, E.; Cai, S.; Jia, H.; Chen, J.; Liang, P. In situ pyrolysis of Ce-MOF to prepare CeO_2 catalyst with obviously improved catalytic performance for toluene combustion. *Chem. Eng. J.* **2018**, *344*, 469–479. [CrossRef]
70. Zhang, Y.-C.; Han, C.; Gao, J.; Pan, L.; Wu, J.; Zhu, X.-D.; Zou, J.-J. NiCo-Based Electrocatalysts for the Alkaline Oxygen Evolution Reaction: A Review. *ACS Catal.* **2021**, *11*, 12485–12509. [CrossRef]
71. Zhang, Q.; Mo, S.; Chen, B.; Zhang, W.; Huang, C.; Ye, D. Hierarchical Co_3O_4 nanostructures in-situ grown on 3D nickel foam towards toluene oxidation. *Mol. Catal.* **2018**, *454*, 12–20. [CrossRef]
72. Mo, S.; Li, S.; Xiao, H.; He, H.; Xue, Y.; Zhang, M.; Ren, Q.; Chen, B.; Chen, Y.; Ye, D. Low-temperature CO oxidation over integrated penthorum chinense-like $MnCo_2O_4$ arrays anchored on three-dimensional Ni foam with enhanced moisture resistance. *Catal. Sci. Technol.* **2018**, *8*, 1663–1676. [CrossRef]
73. Xie, S.; Deng, J.; Zang, S.; Yang, H.; Guo, G.; Arandiyan, H.; Dai, H. Au–Pd/3DOM Co_3O_4: Highly active and stable nano-catalysts for toluene oxidation. *J. Catal.* **2015**, *322*, 38–48. [CrossRef]
74. Janjua, M.R.S.A. Synthesis of Co_3O_4 Nano Aggregates by Co-precipitation Method and its Catalytic and Fuel Additive Applications. *Open Chem.* **2019**, *17*, 865–873. [CrossRef]
75. Xiong, Y.; Zhao, Y.; Qi, X.; Qi, J.; Cui, Y.; Yu, H.; Cao, Y. Strong Structural Modification of Gd to Co_3O_4 for Catalyzing N_2O Decomposition under Simulated Real Tail Gases. *Environ. Sci. Technol.* **2021**, *55*, 13335–13344. [CrossRef]
76. Nosé, S. A unified formulation of the constant temperature molecular-dynamics methods. *J. Chem. Phys.* **1984**, *81*, 511–519. [CrossRef]
77. Hoover, W.G. Canonical dynamics: Equilibrium phase-space distributions. *Phys. Rev. A* **1985**, *31*, 1695–1697. [CrossRef]
78. Hubbard, J.; Flowers, B.H. Electron correlations in narrow energy bands. *Proc. Roy. Soc. Lond. Math. Phys. Sci.* **1963**, *276*, 238–257. [CrossRef]
79. Goedecker, S.; Teter, M.; Hutter, J. Separable dual-space Gaussian pseudopotentials. *Phys. Rev. B Condens. Matter Mater. Phys.* **1996**, *54*, 1703–1710. [CrossRef]